nature communications

Article

https://doi.org/10.1038/s41467-024-51118-x

Graphene-skinned alumina fiber fabricated through metalloid-catalytic graphene CVD growth on nonmetallic substrate and its mass production

Received: 29 January 2024

Accepted: 29 July 2024

Published online: 09 August 2024

Check for updates

Wenjuan Li[1,2,6], Fushun Liang[1,2,6], Xiucai Sun[2,6], Kangyi Zheng[2,3], Ruojuan Liu[1,2], Hao Yuan[1,2], Shuting Cheng[2,4], Jingnan Wang[2], Yi Cheng[1], Kewen Huang[1], Kun Wang[1], Yuyao Yang[1,2], Fan Yang[1,2], Ce Tu[2], Xinyu Mao[2], Wanjian Yin[2,3], Ali Cai[2], Xiaobai Wang[5], Yue Qi[2] ✉ & Zhongfan Liu[1,2] ✉

Graphene growth on widely used dielectrics/insulators via chemical vapor deposition (CVD) is a strategy toward transfer-free applications of CVD graphene for the realization of advanced composite materials. Here, we develop graphene-skinned alumina fibers/fabrics (GAFs/GAFFs) through graphene CVD growth on commercial alumina fibers/fabrics (AFs/AFFs). We reveal a vapor-surface-solid growth model on a non-metallic substrate, which is distinct from the well-established vapor-solid model on conventional non-catalytic non-metallic substrates, but bears a closer resemblance to that observed on catalytic metallic substrates. The metalloid-catalytic growth of graphene on AFs/AFFs resulted in reduced growth temperature (~200 °C lower) and accelerated growth rate (~3.4 times faster) compared to that obtained on a representative non-metallic counterpart, quartz fiber. The fabricated GAFF features a wide-range tunable electrical conductivity (1-15000 Ω sq^{-1}), high tensile strength (>1.5 GPa), lightweight, flexibility, and a hierarchical macrostructure. These attributes are inherited from both graphene and AFF, making GAFF promising for various applications including electrical heating and electromagnetic interference shielding. Beyond laboratory level preparation, the stable mass production of large-scale GAFF has been achieved through a home-made roll-to-roll system with capacity of 468-93600 m^2/year depending on product specifications, providing foundations for the subsequent industrialization of this material, enabling its widespread adoption in various industries.

Chemical vapor deposition (CVD) growth of graphene on catalytic metallic substrates, such as Cu[1–3] and Ni[4–6], stands out as a promising strategy for mass production of high-quality graphene. However, for subsequent applications, the graphene films produced in this manner always require transfer onto target substrates (typically dielectrics or insulators). This transfer process is characterized by its complexity, time-consuming nature, and cost-ineffectiveness[7,8]. In addition, wrinkles, cracks, and contamination are unavoidably introduced into graphene during the transfer process, significantly compromising the intrinsic properties of graphene[8,9]. To enhance the usability and

A full list of affiliations appears at the end of the paper. ✉e-mail: qiyue@bgi-graphene.com; zfliu@pku.edu.cn

processability of atomically thin CVD graphene, an advantageous strategy has been proposed, which is to grow graphene directly on target dielectric/insulating substrates for subsequent transfer-free applications[10–16]. This strategy can circumvent the complex transfer process required for the aforementioned CVD-grown graphene on metal substrates before applications. Additionally, it allows the atomically thin graphene to be integrated into macroscopic material carriers facilitating its transition to practical applications. Clearly, the selection of substrates for graphene CVD growth is crucial for implementing this transfer-free strategy. The chosen substrate will predominantly influence the structure and properties of the resulting graphene composite materials.

Alumina fiber (AF) and its fabric (AFF) represent commercially available engineering materials renowned for their lightweight, flexibility, high strength, and exceptional high-temperature resistance (>1200 °C). These properties have led to their extensive applications as structural reinforcement and thermal insulation materials in diverse fields such as aerospace, wind energy utilization, and architectural engineering[17,18]. Given its properties and distinctive structure, AF/AFF emerges as a promising substrate choice for graphene CVD growth. The integration of graphene with AF/AFF holds the potential to overcome the limitations associated with the atomic-scale thickness of graphene in both processing and applications. This combination is anticipated to unlock innovative opportunities for practical applications of graphene.

In this study, graphene-skinned alumina fiber (GAF) and its corresponding fabric (GAFF) were first developed by CVD growing graphene on the commercial AF and AFF, predominantly composed of γ-Al_2O_3 (referred to as γ-Al_2O_3-AF or -AFF). During the preparation of GAF, the vapor-surface-solid (VSS) growth model of graphene was first revealed on a nonmetallic substrate. This model differs significantly from the conventional vapor-solid (VS) growth model observed on typical non-catalytic nonmetallic substrates[19,20], like quartz[21–23], sappihre[24], *h*-BN[25–27], etc., Instead, it bears a closer resemblance to the graphene growth observed on catalytic metal substrates[8,19]. Indeed, during graphene CVD growth on traditional nonmetallic substrates, the substrate primarily serves as support for graphene layers, with minimal involvement in carbon precursor adsorption, decomposition, and graphene domain growth[19,22]. In contrast, when it comes to graphene growth on catalytic metal substrates, the substrate plays a more active role. It promotes the dissociation of carbon precursors, leading to the generation of active carbon species. These species then feed graphene nucleation and domain growth with the assistance of substrate catalysis. Interestingly, even though γ-Al_2O_3-AF is a nonmetallic substrate, it exhibits remarkable catalytic capacities for the series of elementary steps involved in graphene CVD growth. The low-coordination aluminum atoms in γ-Al_2O_3-AF serve multiple crucial roles in graphene growth process. Firstly, these atoms can facilitate the adsorption and decomposition of carbon precursors, thereby promoting graphene nucleation. Additionally, they aid in the attachment of active carbon species at graphene edges and subsequently facilitate the detachment of hydrogen (H) during domain growth. These functions underscore the remarkable catalytic properties of γ-Al_2O_3-AF in the graphene CVD growth process. As a result, the VSS growth model of graphene on γ-Al_2O_3-AF has significant implications. It enables graphene growth at a much-reduced temperature (~200 °C lower) and a much faster growth rate (~3.4 times faster) compared with that on conventional catalytically-inert nonmetallic substrates, like quartz fiber (QF), which is the representative comparison counterpart for γ-Al_2O_3-AF in terms of the structure, dimension, and component. The obtained GAFF successfully inherited the structural and functional properties of its constituent materials. It displayed a wide-range adjustable electrical conductivity (spanning from 1 to 15,000 Ω sq^{-1}), high tensile strength (>1.5 GPa), lightweight, flexibility, and a hierarchical macrostructure. This indicates the successful integration of graphene with AFF, endowing GAFF with a diverse range of desirable attributes suitable for various applications. As a result, GAFF exhibits promising applications across various fields, such as electrical heating and electromagnetic interference (EMI) shielding. Moreover, beyond the laboratory-level preparation of GAFF, stable mass production of large-scale GAFF has been achieved through a home-made continuous roll-to-roll CVD system, with an annual capacity ranging from 468 to 93,600 m^2 depending on specifications of products. Such scalability provides a solid foundation for the industrialization of this material, paving the way for its widespread adoption in practical applications.

Results

Preparation of GAF

The CVD strategy was applied for graphene growth on γ-Al_2O_3-AF to realize the conformal coverage of continuous graphene layers on each fiber (Fig. 1a (left)). The commercially obtained γ-Al_2O_3-AF was composed of ~72% γ-Al_2O_3 and ~28% amorphous SiO_2 (a-SiO_2), as illustrated in Fig. 1a (right) (see more details in Supplementary Fig. 1). Notably, the microstructure and composition of AF remained unchanged after ~1050 °C heating for ~2 h (Fig. 1b and Supplementary Fig. 2), which was well compatible with the high-temperature growth conditions of CVD graphene. Figure 1c showed the photograph of the fabricated GAF, where the featured fiber-shaped structure was well maintained after graphene growth, as well as the flexibility and strength, which will be further illustrated later. The uniform contrasts in the scanning electron microscopy (SEM) (Fig. 1d) and the uniform Raman 2D peak mapping (Fig. 1e) of GAF confirmed the continuous conformal full coverage of graphene layers on each fiber. The Raman spectra in Fig. 1f were collected from 10 evenly-spaced positions on GAF, as marked in Fig. 1c, which showed the uniform I_D/I_G (intensity ratio of D and G peaks) and I_{2D}/I_G (intensity ratio of 2D and G peaks) (see more details in Supplementary Table 1), further confirming the excellent uniformity of graphene on the fiber surface.

To measure the thickness of graphene, the AF core in GAF was etched in hydrofluoric acid (see more details in Methods), where graphene layers covered on the fiber collapsed onto the silicon substrate forming graphene ribbons. The measured thickness of the ribbon was twice the actual thickness of the grown graphene. Figure 1g showed the AFM image of the graphene ribbon obtained, presenting the thickness of ~2.6 nm, corresponding to ~3 layers of graphene, which was well consistent with the High resolution-transmission electron microscope (HR-TEM) characterization in Fig. 1h, where the graphene stacking layers can be clearly observed. In addition, the selected-area electron diffraction (SAED) (Fig. 1i) revealed the polycrystalline structure of graphene, further confirming the high crystal quality of graphene obtained on this nonmetallic substrate. In addition, the thickness of graphene layers in GAF can be effectively modulated by regulating growth conditions, such as growth time (see more details in Supplementary Fig. 3). For example, under the same growth conditions as that in Fig. 1g, when the growth time was modulated to ~70, ~75, and ~90 min, the obtained thicknesses of graphene layers were ~1, ~2, and ~5, respectively.

Distinctive growth behaviors of graphene on γ-Al_2O_3-AF

To clarify graphene growth behaviors on this γ-Al_2O_3-AF, the different growth stages of graphene on this substrate were detailed inspected. In addition, in order to compare the underlying CVD growth mechanisms of graphene on AF with that on traditional nonmetallic substrates, QF (>99.9% SiO_2), was also introduced parallelly as the graphene growth substrate. Quartz is a typical nonmetallic substrate widely used for graphene CVD growth, where graphene growth behaviors have been clarified by many works[13,28–30]. On the catalytically inert nonmetallic quartz substrate, graphene CVD growth followed the well-known VS model[19,23], where the substrate played minor roles in carbon precursor adsorption and decomposition, as well as graphene domain growth. Consequently, graphene growth on quartz substrate usually suffered from the limited growth rate and high temperature required. The previously reported works by our group have also

https://doi.org/10.1038/s41467-024-51118-x

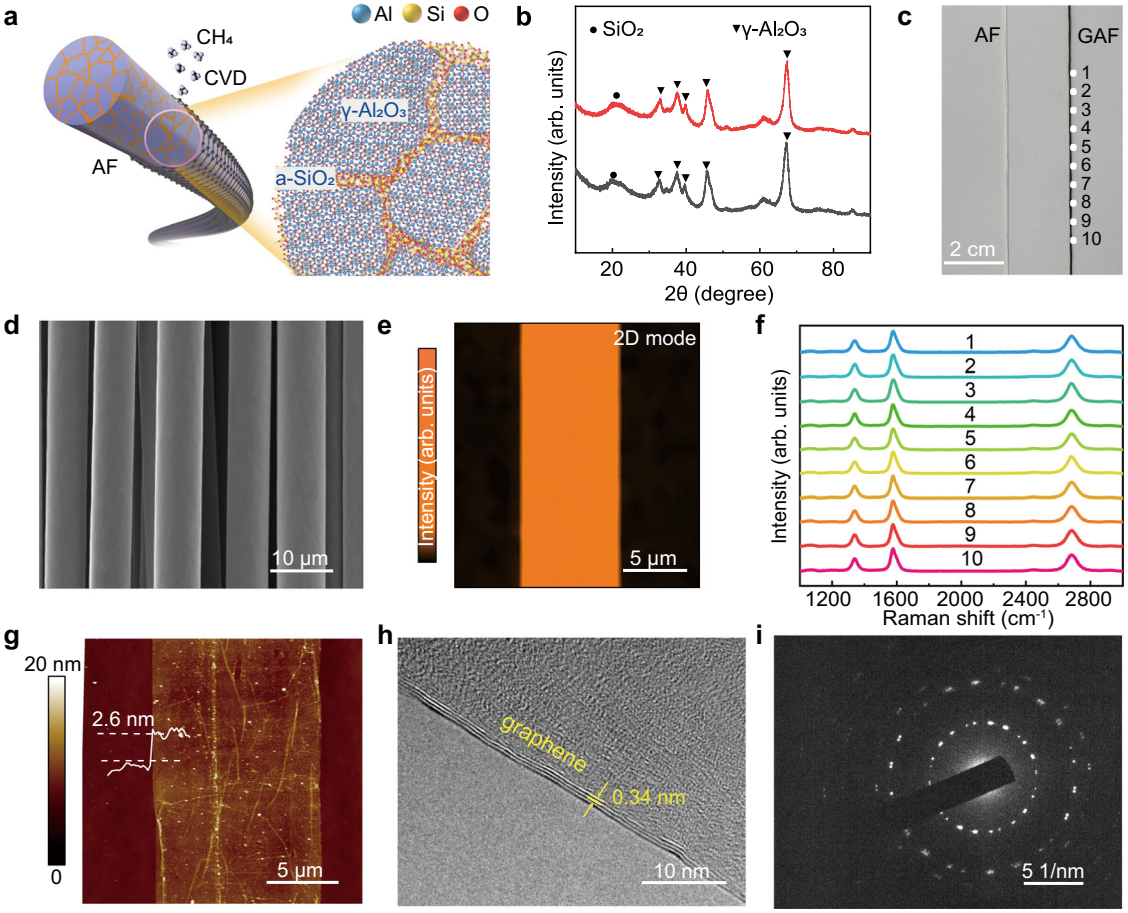

Fig. 1 | Preparation and characterizations of graphene-skinned alumina fiber (GAF). a Schematic of GAF prepared via chemical vapor deposition (CVD) process, and the structure of AF consisting of ~72% γ-Al_2O_3 and ~28% amorphous SiO_2 (a-SiO_2). **b** X-ray diffraction (XRD) patterns of pristine AF and the annealed AF at ~1050 °C for ~2 h. **c** Photograph of AF (left) and GAF (right). **d**, **e** SEM image (**d**) and Raman mapping (**e**) of GAF in **c**. **f** Raman spectra from 10 evenly-spaced positions on GAF as marked in **c**. **g** Atomic force microscope (AFM) image of graphene ribbon obtained after etching AF core of GAF in **c**, the height profile showed the height value was ~2.6 nm. **h**, **i** High resolution-transmission electron microscope (HR-TEM) image of 3-layer graphene on AF (**h**), and corresponding selected area electron diffraction (SAED) patterns (**i**). Growth conditions in **c**-**i**: 500 sccm Ar, 200 sccm H_2, 20 sccm CH_4, target temperature of ~1050 °C, growth time of ~80 min, see more details in "Methods" section.

revealed the graphene CVD growth on QF, which further confirmed the lack of catalytic capability of this substrate[10,11,31,32]. To provide systematic comparisons with graphene growth behaviors on AF, graphene growth on QF was also conducted under the same gas flow and growth temperature as that on AF in Fig. 1. As shown in Supplementary Fig. 4, the morphology of QF substate was well maintained after the high-temperature deposition of graphene. The comparative results show that obtaining a similar thickness of graphene layers requires significantly more time on QF than on AF, and the obtained graphene layers on QF feature lower quality than that obtained on AF. These differences imply the distinct growth behaviors for graphene on QF and AF and the facilitation of AF substrate for graphene growth, which will be further discussed in Figs. 2 and 3.

The CVD growth of graphene is considered as a kinetic process, in which precursors can diffuse toward the edge and attach to the active sites on the edge by overcoming the attachment barrier. Meanwhile, every atom at the edge of the two-dimensional crystal presented a possibility to escape into the environment[33]. The incubation time in graphene CVD growth process refers to the period in which carbon species from precursor decomposition accumulate on the substrate surface to reach a critical supersaturation level to overcome the energy barrier for graphene nucleation[34,35]. As shown in Fig. 2a (top), SEM images showed that a large number of graphene nuclei have already formed within ~20 min on AF. In contrast, no domain appeared on the QF surface even after the feedstock supply by ~60 min, and at ~120 min, graphene domains were observed (Fig. 2a, bottom and Supplementary Fig. 5), which indicated the much longer incubation time required for graphene nucleation on QF than that on AF. Figure 2b showed the nucleus density of graphene on AF and QF, both of which showed the linear increase as the function of growth time (t). In addition, the nucleation time (t_0) can be calculated by linear fitting extrapolation, as marked by star symbols in Fig. 2b. The estimated t_0 for graphene nucleation was ~4 and ~80 min on AF and QF, respectively, which implied that the much faster nucleation on AF. It is worth mentioning that the nucleation of graphene on metal substrates can be completed within a few seconds[2,36], while the nucleation time on the non-catalytic substrates usually takes up to tens of minutes[13,29], consistent with that observed on QF in this work. It can be noticed that the nucleation time of graphene on AF is an order of magnitude between that of metal and quartz. This implied that in graphene CVD growth, AF substrate might not behave like the traditional non-catalytic nonmetallic substrates, such as quartz and sapphire, but more like the catalytic metal substrates in promoting graphene nucleation. Therefore, the possible metalloid catalytic properties may be possessed by this γ-Al_2O_3-AF, which will be further discussed in Fig. 3. In Fig. 2b, the slopes of the linear fitting curves correspond to the nucleation rate of graphene. The nucleation rate of graphene on AF was much faster (~0.90 nuclei μm^{-2} min^{-1}) than that on QF (~0.24 nuclei μm^{-2} min^{-1}). After the nucleation, graphene

https://doi.org/10.1038/s41467-024-51118-x

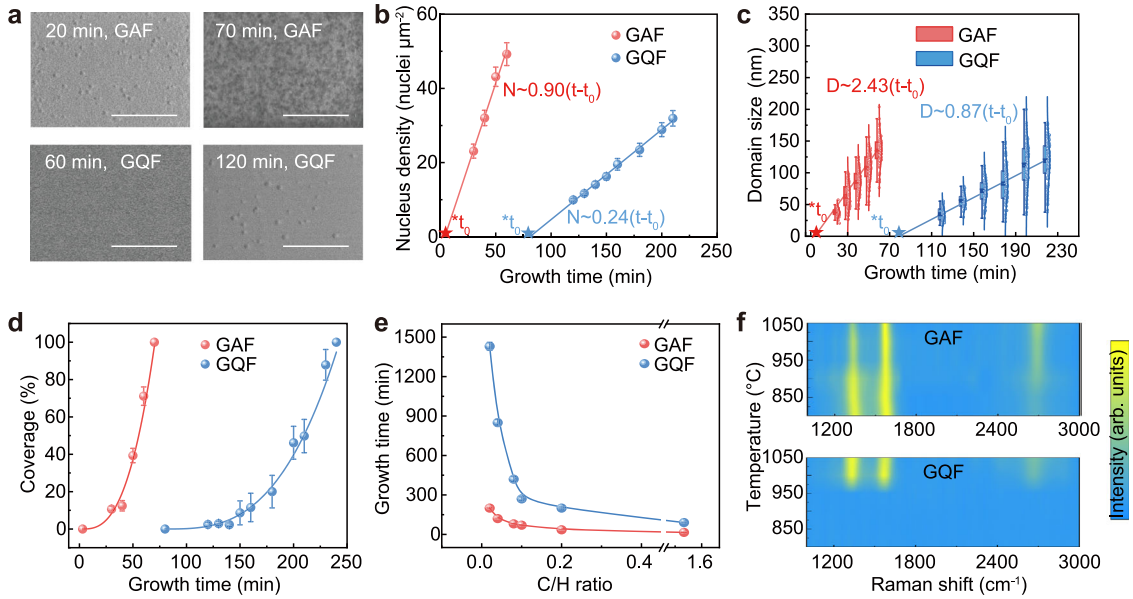

Fig. 2 | Comparisons of graphene CVD growth behaviors on alumina fiber (AF) and quartz fiber (QF). a SEM images of GAF obtained with the growth time of ~20 and ~70 min (top), and graphene-skinned quartz fiber (GQF) obtained with the growth time of ~60 and ~120 min (bottom). Scale bar, 1 μm. **b**, **c** Graphene nucleus densities (*N*) (**b**) and domain size (*D*) (**c**) obtained on AF and QF with various growth time. The linear fitting was in the form of $N/D = k(t\text{-}t_0) + b$, where the slope *k* was the nucleation rate (**b**) or growth rate of domains (**c**), *t* (≥t_0) and t_0 were the growth and nucleation time, respectively, and b was the constant. **d** Coverage changing of graphene on AF and QF as a function of growth time. The nonlinear fitting was in the form of $A = \sum A_i \sim a(t - t_0)^3$, where *A*, A_i, *a*, *t*, and t_0 represent the total coverage, area of each graphene domain, the coefficient of the nonlinear fitting, growth time and nucleation time. Growth conditions in **a**–**d**: 500 sccm Ar, 200 sccm H_2, 20 sccm CH_4, target temperature of ~1050 °C with changing growth time. **e**, Growth time consumed to realize the full coverage of graphene layers on AF and QF at various C/H ratios (growth conditions: 500 sccm Ar, 200 sccm H_2, with various C/H ratios of 0.02, 0.04, 0.08, 0.10, 0.20, and 1.50 under the target temperature of ~1050 °C). **f** Raman spectra of GAF (top) and GQF (bottom) obtained at different growth temperatures of ~800, ~850, ~900, ~950, ~1000, and ~1050 °C (growth conditions: 500 sccm Ar, 200 sccm H_2, 20 sccm CH_4, with the growth time of ~200 min under above growth temperatures).

domains kept growing. As shown in Fig. 2c, to obtain the equal domain size, graphene growth on AF consumed a much shorter time than that on QF, where the growth rate of domains on AF (the slope of the linear fitting curve) was estimated to be ~2.43 nm min^{-1}, nearly three times as fast as that on QF (~0.87 nm min^{-1}). And t_0 on AF and QF obtained in Fig. 2c was well consistent with that obtained in Fig. 2b.

The combination of the faster nucleation and domain growth rates for graphene on AF than that on QF resulted in a much faster increase in the total graphene coverage, which was equal to the sum of the entire graphene domain area on the surface. As the reaction proceeded, graphene domains gradually coalesced to form continuous graphene films fully covering the fiber surface. It can be noticed in Fig. 2d that it took ~70 min to realize the full coverage of graphene on AF, while ~240 min was consumed on QF. From the nonlinear fitting in Fig. 2d, the total coverage was proportional to the cube of the growth time. The expression for total coverage of graphene is defined as:

$$A = \sum A_i \sim a(t - t_0)^3 \quad (1)$$

Where *A*, A_i, *a*, *t*, and t_0 represent the total coverage, area of each graphene domain, the coefficient of the nonlinear fitting, growth time and nucleation time. The calculated values of *a* were 8.7×10^{-4} and 1.7×10^{-5} at AF and QF curves, respectively, indicating that the graphene coverage increased on AF much more quickly than that on QF because of the rapid nucleation and domain growth.

In addition, the growth of graphene on AF can be effectively modulated through growth conditions, such as methane/hydrogen (C/H) ratios. Figure 2e presented that the growth time consumed to achieve the full coverage of graphene on both substrates decreased as the C/H ratios increased. It can be noticed that the growth time required for graphene full coverage on AF was much shorter than that on QF under the series of C/H ratios. Moreover, the critical growth temperature required for graphene formation was a vital parameter to evaluate the catalytic capacity of the growth substrate. Figure 2f presented Raman spectra of graphene grown on AF (top) and QF (bottom) at the growth temperature of 800–1050 °C under the same growth conditions (see more growth details in Supplementary Fig. 6). The G band in Raman spectrum of graphene is usually used to determine the formation of sp^2 carbon[37]. Notably, the G peak of graphene on AF can be detected at ~800 °C, ~200 °C lower than that on QF, which implies the facilitating effects of γ-Al_2O_3 on graphene CVD growth.

Vapor-surface-solid growth model of graphene on γ-Al_2O_3-AF

Figure 2 revealed the distinctive growth behaviors of graphene on γ-Al_2O_3-AF from that on traditional non-catalytic nonmetallic substrates. To understand the role of γ-Al_2O_3 in graphene growth and give a comprehensive understanding of the growth model, the theoretical calculations related to precursor adsorption and decomposition, as well as domain growth, were conducted in Fig. 3. Meanwhile, the quartz substrate was also included for comparison.

In Fig. 3a, the density functional theory (DFT) calculations for the adsorption energies (E_{ads}) of CH_4 on γ-Al_2O_3 and SiO_2 surfaces were conducted to evaluate the interactions of the carbon precursor with the growth substrates. According to previous explorations[38,39], (110) is the most stable surface of γ-Al_2O_3, and is the main plane of γ-Al_2O_3 crystal, so γ-Al_2O_3 (110) was selected as a representative model to investigate graphene CVD growth on γ-Al_2O_3-AF (Supplementary Fig. 7). For quartz substrate, SiO_2 (0001) surface was usually used for theoretical calculations due to its high stability, which has two typical surfaces, *i.e.* Si- and O-terminated SiO_2 (0001) (Supplementary Fig. 8)[10,11,40,41]. In this way, Si- and O-terminated SiO_2 (0001) surfaces were chosen as the representative surfaces for the quartz substrate. As shown in Fig. 3a and Supplementary Fig. 9, the E_{ads} of CH_4 on γ-Al_2O_3 was significantly lower than that on SiO_2, suggesting γ-Al_2O_3 can

https://doi.org/10.1038/s41467-024-51118-x

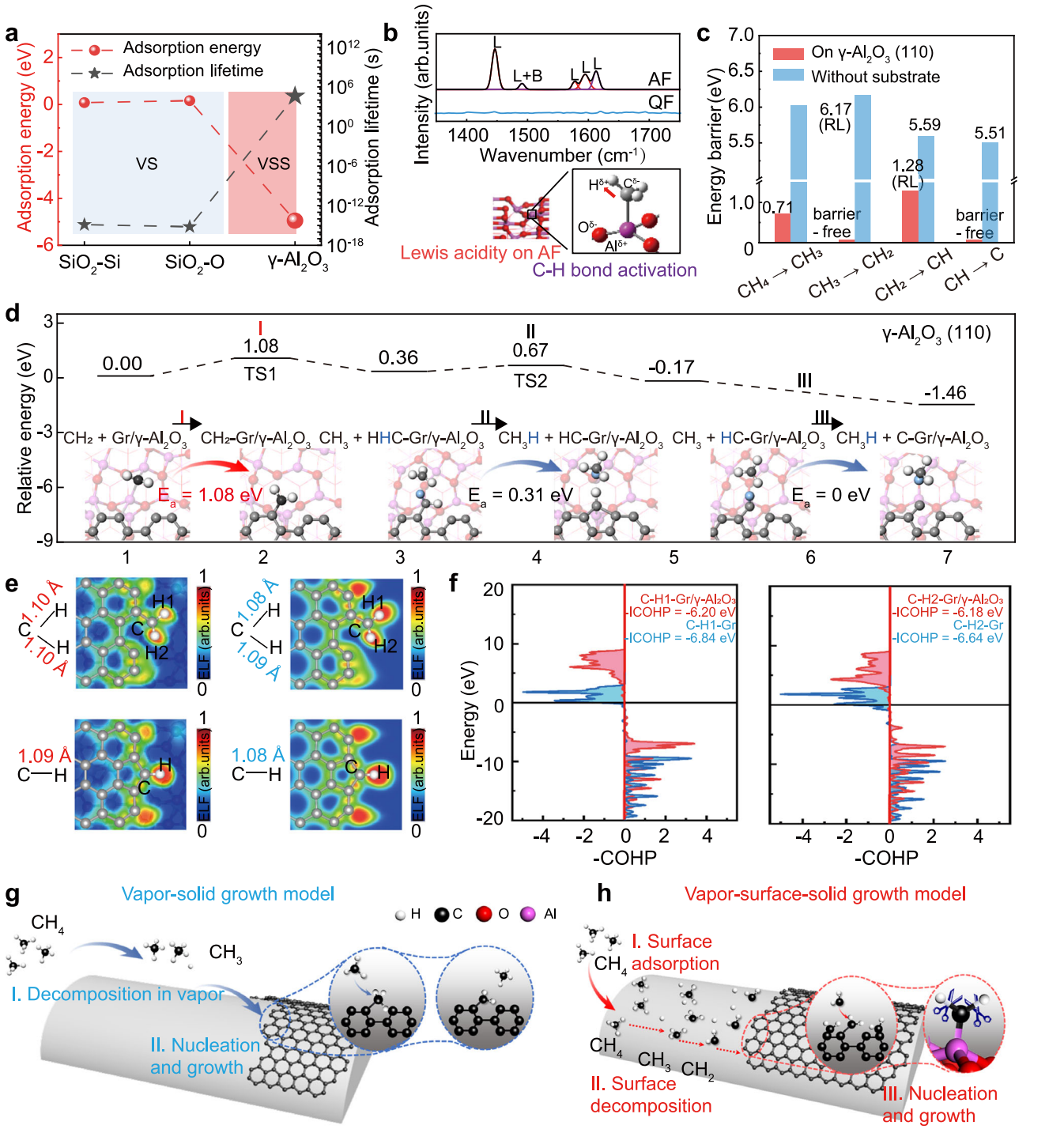

Fig. 3 | CVD growth mechanisms of graphene on γ-Al_2O_3-AF. a Comparisons of adsorption energy and lifetime of CH_4 on Si- and O-terminated SiO_2 (0001) surface (SiO_2-Si and SiO_2-O, respectively), and γ-Al_2O_3 (110) surface. **b** Fourier transform-infrared (FT-IR) spectra of pyridine adsorbed on AF and QF (top), and schematic for the structure of Lewis acid site on AF and its interaction with the absorbed hydrocarbon (bottom). L and L + B indicated Lewis and Lewis and Brønsted acid sites, respectively. **c** Comparisons of the energy barriers for CH_4 stepwise decomposition on γ-Al_2O_3 (110) and without substrate supporting, where RL was the rate-limiting step. **d** Kinetic energy profile and atomic configurations for CH_2 species participating in graphene CVD growth on γ-Al_2O_3 (110). TS1 and TS2 were transition states 1 and 2, respectively, and represented arrows indicated the processes of reactions I, II, and III. **e** C−H bond lengths and electron localization function (ELF) diagrams of CH_2-Gr and CH-Gr at growing graphene edge with (left) and without (right) γ-Al_2O_3 substrate supporting. **f** The -COHP of C−H bonds in CH_2-Gr with (red region) and without (blue region) γ-Al_2O_3 substrate supporting. The two C−H bonds in CH_2-Gr were marked as C-H1-Gr and C-H2-Gr. **g**, **h** Schematics of graphene vapor-solid (VS) growth model on traditional catalytically inert nonmetallic substrates (**g**) and graphene vapor-surface-solid (VSS) growth model on γ-Al_2O_3-AF (**h**).

capture CH_4 precursor more easily. Furthermore, the adsorption lifetime ($\tau = \tau_0 \exp(-E_{ads}/k_aT)$) of CH_4 on the SiO_2 surface ranged from 10^{-16} to 10^{-15} s. Such a short adsorption lifetime was not sufficient for CH_4 to proceed with the subsequent surface reactions, suggesting the conventional VS graphene growth model on the quartz substrate. In contrast, the CH_4 adsorption lifetime on γ-Al_2O_3 surface was as long as ~10^4 s, which is the important premise for the subsequent series surface reactions, like the surface-catalytic decomposition of precursor and

graphene nucleation, much similar to the typical VSS growth model of graphene on catalytic metal substrates[8,19].

In addition to the enhanced adsorption of carbon precursor on the surface of γ-Al_2O_3-AF, the substrate also imposed obvious promotion for the decomposition of the adsorbed precursors. According to the reported works[42–45], the Lewis acid functionality of γ-Al_2O_3 can catalyze the C–H cleavage of hydrocarbons through the electrostatic interactions. The pyridine-adsorbed FT-IR (Py-IR) spectra can reveal the acid sites on the substrate surface. Figure 3b (up) showed the Py-IR of γ-Al_2O_3-AF, where the bands at ~1445, ~1575, ~1593, and ~1614 cm^{-1} were attributed to the Lewis acid sites, and the band at ~1490 cm^{-1} was derived from the Lewis and Brønsted acid sites. In contrast, there was no obvious acid site observed on the QF surface. Specifically, as schematically shown in Fig. 3b (bottom), the centers of Lewis acid sites on γ-Al_2O_3 were located at Al atoms with low coordination, such as tri-coordinated and tetra-coordinated, which were electron-deficient and can impose the electron-pulling effect on the absorbed hydrocarbon, causing its electron cloud shifting and facilitating C–H bond breaking[42–45]. Consequently, the dehydrogenation energy barrier of carbon species absorbed on the surface of γ-Al_2O_3-AF can be largely decreased, and the highly dissociated active carbon species will be produced for subsequent graphene growth. Figure 3c and Supplementary Fig. 10 presented the comparisons of the energy barriers for CH_4 stepwise decomposition on γ-Al_2O_3 (110) surface and without substrate supporting. Obviously, the energy barrier of each decomposition step of CH_4 on γ-Al_2O_3 (110) surface was much lower than that without substrate. And the barrier of the rate-limiting (RL) step of CH_4 decomposition on γ-Al_2O_3 (110) (CH_2→CH + H) was only ~1.28 eV, significantly lower than that without substrate supporting (~6.17 eV for CH_3→CH_2 + H). This indicated that the γ-Al_2O_3 (110) surface can significantly activate the C–H bonds in CH_4, and trigger the chain reaction of decomposition with low energy. It was noted that the rate-limiting step for CH_4 decomposition on γ-Al_2O_3 (110) surface occurred in the third step, in contrast to the second step for the decomposition without substrate, and the decomposition energy for CH_3→CH_2 + H on γ-Al_2O_3 (110) surface was barrier-free, which was favorable for the production of highly-dehydrogenated CH_2. Consequently, CH_2 was regarded as the main active carbon species after CH_4 decomposition on γ-Al_2O_3 (110), which much favors the edge graphitization and growth acceleration of graphene. In the calculations related to graphene edge growth, the attachment of CH_2 was investigated.

The kinetic process of graphene CVD growth on γ-Al_2O_3 (110) surface was theoretically simulated in Fig. 3d. The configuration of armchair (AC) terminated graphene edge (AC-Gr) was much more stable than zigzag (ZZ) terminated edge (ZZ-Gr) on γ-Al_2O_3 (110) surface (Supplementary Fig. 11), therefore AC-Gr was chosen for the kinetic process explorations, and each carbon atom exposed at the AC edge of graphene can be considered equivalent for monomer attachment. As analyzed in Fig. 3c and Supplementary Fig. 10, CH_2 was the main active carbon species from CH_4 decomposition on γ-Al_2O_3 (110) surface, so the process of CH_2 attachment to the growing graphene edges was investigated. As shown in Fig. 3d, the kinetic process of graphene edge extension can be regarded as a continuous attachment of CH_2 at the graphene edge to form CH_2-Gr and the subsequent removal of H atoms in CH_2-Gr (edge graphitization). The threshold step in the process was the CH_2 attachment with an energy barrier of ~1.08 eV. Notably, this value was much lower than the corresponding threshold reaction barrier on the traditional non-metallic substrates, such as quartz and sapphire (~3.00 eV)[19], which implied that CH2 attachment to graphene edges was easier to proceed on γ-Al2O3 (110). After CH_2 attachment, the dehydrogenation of CH_2-Gr followed. To further explore the effects of γ-Al_2O_3 on the dehydrogenation process in CH_2-Gr, the configurations and electronic characteristics of the C–H bonds were analyzed in Fig. 3e. The C–H bond lengths of CH_2-Gr and CH-Gr on γ-Al_2O_3 were much longer than that without substrate supporting. In addition, the electron localization function (ELF) at graphene edges was also calculated, which indicated the degree of electron localization and reflected the difficulty of the formation and breaking of the chemical bonds. ELFs of C–H in CH_2-Gr and CH-Gr on γ-Al_2O_3 were obviously lower than that without substrate support, indicating the easier detachment of H atoms from graphene edges under the assistance of γ-Al_2O_3 substrate. Figure 3f shows the negative crystal orbital Hamilton population (-COHP) of C–H bonds in CH_2-Gr with and without γ-Al_2O_3 substrate support. The integrated -COHP (-ICOHP) can reflect the strength of the C–H bond, a higher absolute value implying the stronger covalent bond. It can be found that the absolute value of -ICOHP of C–H bond in CH_2-Gr on γ-Al_2O_3 was lower than that without γ-Al_2O_3 supporting, indicating the participation of γ-Al_2O_3 substrate can significantly weaken the C–H bond strength and facilitate H detachment at growing graphene edges.

Generally, graphene growth on the catalytically inert nonmetallic substrates usually complied with the VS growth model[19,23], where the nonactive substrate played negligible roles in promoting graphene CVD growth. In contrast, the catalytic metallic substrates, such as Cu and Ni, presented the excellent catalytic capability for the series of elementary steps of graphene growth, including the carbon precursor adsorption and decomposition on the substrate, attachment of active carbon species at growing graphene edges, as well as the subsequent dehydrogenation of CH_2-Gr for domain extending[23,46]. Due to the active surface, it experienced a VSS process, which can be demonstrated as a VSS growth model. According to the theoretical analyses in Fig. 3, instead of the VS model on the traditional nonmetallic substrates (Fig. 3g), graphene CVD growth on γ-Al_2O_3-AF showed the typical features of the VSS model (Fig.3h), which resulted in the relatively low growth temperature and fast growth rate as experimentally observed in Fig. 2.

Graphene CVD growth on γ-Al_2O_3 has indeed been previously reported[44,47–49], which provided us valuable references. However, upon a thorough examination of relevant works, there are significant distinctions between our study and those reported works. For example, Yong-Won Song et al. achieved graphene CVD growth on γ-Al_2O_3 substrate[44]. However, our study exhibits significant differences from theirs in terms of investigation of growth processes, construction of growth model, and conduction of theoretical calculations. Additionally, the works of Roman Ivanov et al. and Ali Saffar Shamshirgar et al. reported the preparation of composites of graphene and γ-Al_2O_3 nanofibers by CVD method[47,48]. Both works primarily focused on the properties and applications of the resulting composites without delving into the detailed growth behaviors of graphene on γ-Al_2O_3. In addition, their obtained graphene-alumina composites are quite different from GAFF in macroscopic appearance, which leads to distinct application scenarios and proposes different requirements for their scale-up strategies. Moreover, Qi Zhao et al.'s work investigated CH_4^* dissociation and $C_nH_{2n}^*$ (n = 2–6) formation on γ-Al_2O_3[49], which carefully examined the initial stages of graphene CVD growth, including carbon precursor decomposition and intermediate formation, while the other important elementary steps in graphene CVD growth progress were not discussed. Further experimental work was somehow lacking to verify the theoretical results. Our study represents a full-spectrum development of a material, GAFF, from the proposal of preparation method to the establishment of growth model, development of large-scale progress and equipment, and demonstration of practical applications. Therefore, our study exhibits significant distinctions from previously reported works, and provides comprehensive experimental and theoretical evidences to support the proposition of the explicit VSS growth model for CVD graphene on γ-Al_2O_3.

Lightweight, flexible, high-strength, conductive GAFF

GAFF was fabricated through graphene CVD growth on commercial AFF, as schematically shown in Fig. 4a, and Fig. 4b exhibits the

https://doi.org/10.1038/s41467-024-51118-x

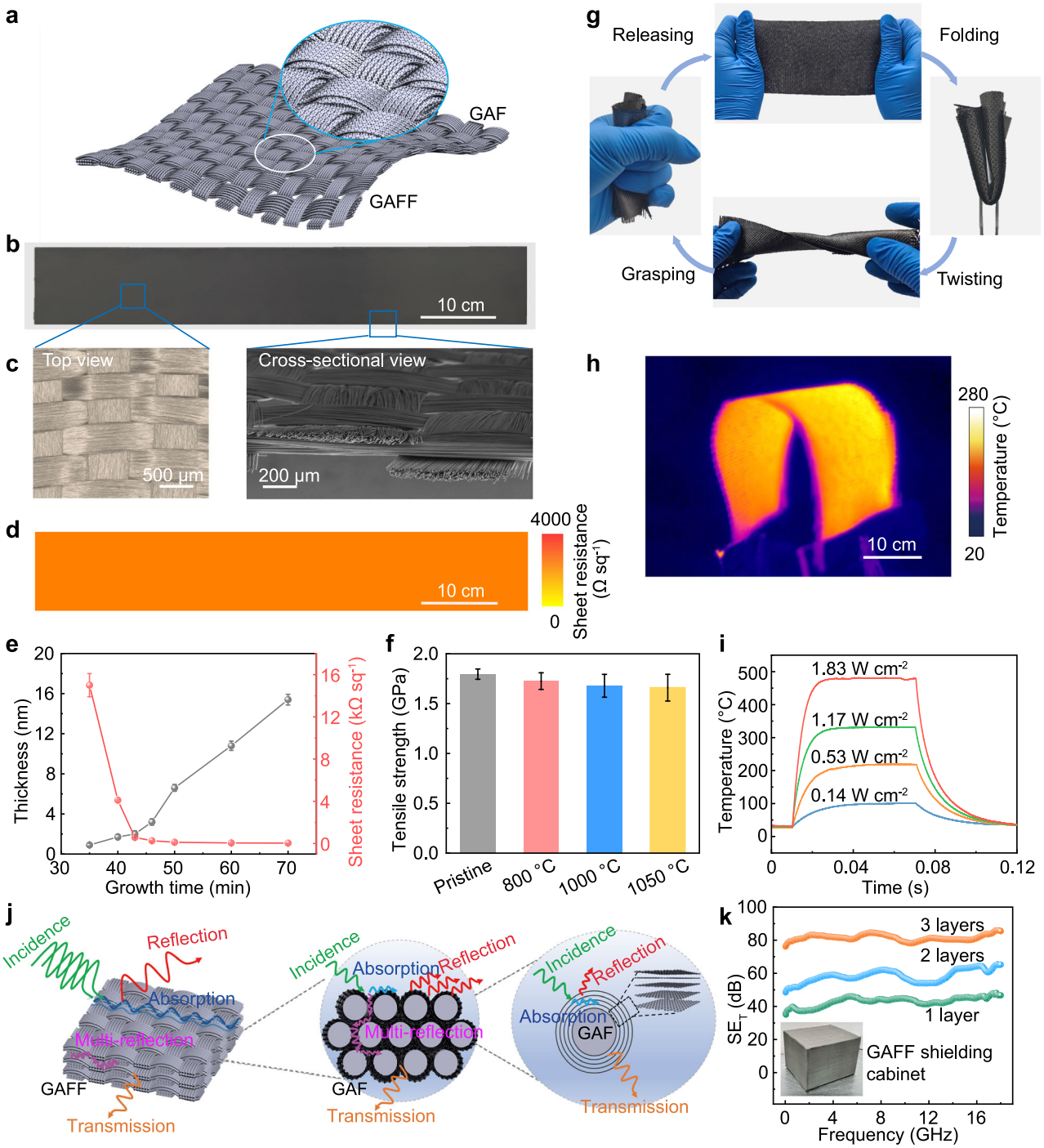

Fig. 4 | Electrical and mechanical properties of GAFF. a, **b** Schematic (**a**) and photograph (**b**) of GAFF. **c** Top-view optical microscope images of GAFF (left) and SEM of the cross-sectional of GAFF (right). **d** Sheet resistance mapping of GAFF. **e** Wide range of sheet resistance of GAFF obtained by modulating graphene thickness, which was growth-time dependent. Growth conditions: 500 sccm Ar, 200 sccm H_2, and 40 sccm CH_4 with growth time of ~35, ~40, ~45, ~50, ~60, and ~70 min under the target temperature of ~1050 °C. The error bars represent the standard deviations (n = 5). **f** Tensile strength of the pristine AF and GAF obtained at different graphene growth temperatures (~800, ~1000, and ~1050 °C for ~2 h). The error bars represent the standard deviations (n = 5). **g** Photographs of GAFF going through the series of mechanical deformations of grasping, folding, twisting, and releasing. **h** Infrared image of the bent GAFF-based heater (~220.1 ± 3.7 °C, input voltage of ~12 V, 10 cm × 20 cm, sheet resistance of ~2 Ω sq^{-1}). **i** Temperature profiles of GAFF at different power densities. **j** EMI shielding mechanisms in the hierarchical conductive configuration of GAFF. **k** Shielding effectiveness (SE_T) of the GAFF shielding cabinet composed of 1–3 layers of GAFFs (GAFF thickness of ~0.27 mm, sheet resistance of ~2 Ω sq^{-1}). Inset, photograph of GAFF shielding cabinet (20 × 20 × 20 cm^3).

photograph of the obtained large-scale (20 cm × 110 cm) uniform GAFF. The top (left in Fig. 4c) and cross-sectional (right in Fig. 4c and Supplementary Fig. 12) views of GAFF present the clear structure of the fabric woven from warp and weft yarns in a plain texture (with a yarn count of 26 × 26 per inch), and each yarn comprised thousands of fibers with a diameter of ~7 μm. Figure 4d presented sheet resistance mappings of GAFF in Fig. 4b, which showed high conductivity uniformity with the average sheet resistance of 3530.1 ± 50.3 Ω sq^{-1} and a

low variation coefficient of ~0.06 (see more details in Supplementary Fig. 13). Notably, the sheet resistance of GAFF can be effectively modulated in a wide range through graphene thickness regulation, which can be controlled by the growth time of graphene (Fig. 4e) (more details in Supplementary Fig. 14). The modulation for the graphene thickness and the sheet resistance of GAFF is significant, which is the premise to satisfy various application requirements.

AF/AFF presented excellent high-temperature resistance, therefore the damage to its mechanical properties by the CVD process (~800, ~1000, and ~1050 °C for ~2 h) can be nearly negligible (Fig. 4f and Supplementary Figs. 15 and 16), and the tensile strength of GAF was kept >1.5 GPa. In addition, the GAF/GAFF also possessed excellent flexibility. As shown in Fig. 4g, after the multiple grasping, folding, twisting, and releasing (each deformation action was repeated 20 times), the morphology of GAFF presented negligible change and no peeling of graphene layers was observed (Supplementary Fig. 17). Moreover, the effects of mechanical deformations on graphene layers were further characterized by Raman characterization. As shown in Supplementary Fig. 18, after multiple grasping, folding, twisting, and releasing, negligible change was observed in the Raman spectra of graphene, especially I_D/I_G and I_{2D}/I_G, proving that the graphene layers in GAFF can maintain the stable structure after a series of mechanical deformations. In addition, the pristine AFF is featured with a low density of ~2.9 g cm^{-3}, and the obtained GAFF had negligible weight increase after the conductive graphene covering. High-performance graphene layers endow AF/AFF with additional attributes, such as the excellent electrical, electric-heating, and electromagnetic shielding properties (see more details in Supplementary Fig. 19). The lightweight conductive GAFF showed promising application potentials used as a flexible electrothermal heater. Figure 4h displayed the infrared image of the GAFF-based heater (10 cm × 20 cm), which can be bent into various states and keep the uniform temperature distribution (see more details for the construction of GAFF-based heater in "Methods" section). The heating and cooling curves of the GAFF-based heater under different power densities were shown in Fig. 4i. The GAFF-based heater presented a very short response time (time consumed to reach 90% of the saturated temperature) and high heating rate (increasing rate of temperature within the response time), which was mainly attributed to the lower density of the material. For example, at the low input power density of ~1.83 W cm^{-2}, the response time was short to ~8 s and the heating rate can reach ~21 °C s^{-1}. With its exceptional attributes, such as high heating uniformity, rapid heating rate, and controllable heating capability, GAFF emerges as a good material choice for electrothermal applications, such as for electric heating deicing and anti-icing. In addition, GAFF also showcases infrared radiation properties with infrared emissivity and electrothermal radiation conversion efficiency up to ~0.92 and ~40%, respectively (GAFF with sheet resistance of ~30 Ω sq^{-1}) (Supplementary Fig. 20). Therefore, GAFF holds great promise for a wide array of applications within the realm of infrared radiation heating[11,50,51].

AFF is a typical wave-transparent material with high electromagnetic wave (EMW) transmittance (see more details in Supplementary Fig. 19e, f). Graphene covering endows AFF with excellent electrical conductivity, along with electromagnetic interference (EMI) shielding capability. The unique woven structure composed of warp and weft yarns (each containing thousands of fibers) in GAFF constructed the characteristic hierarchical conductive configuration, which brought about the distinctive advantages for applications in EMI shielding. As schematically presented in Fig. 4j, when EMW was incident on GAFF, part of it was reflected due to the interactions with the surface free charge carriers of graphene[52,53] (left of Fig. 4j). Then, the residual EMW entered the inside of the weaving structure of GAFF, where it was multi-reflected between multiple adjacent fibers, and the multi-absorption was accompanied (middle of Fig. 4j). In addition, when multilayers of GAFFs were stacked together, the multi-reflection between GAFFs also occurred to further enhance the EMW loss. More microscopically, when EMW was incident on the single GAF in the fabric, it will be reflected by graphene layers, meanwhile, part of it will be absorbed through the conductivity loss and polarization relaxation loss in graphene layers (right of Fig. 4j). In addition, the effects of stacking angle and configuration of multi-layer stacked GAFFs on the EMI shielding performance have also been explored. Our findings reveal that both stacking angle and configuration have negligible effects on the EMI shielding effectiveness (SE_T) of the stacked GAFFs (Supplementary Fig. 21). Based on GAFF, a shielding cabinet was successfully constructed. As the photograph is shown in Fig. 4f (inset), the size of the GAFF shielding cabinet was 20 × 20 × 20 cm^3, and each surface of the cabinet was covered by GAFF. The tested EMI shielding effectiveness (see more details in Supplementary Fig. 22) showed that the cabinet constructed with 1-layer GAFF (sheet resistance of ~2 Ω sq^{-1}, thickness of ~0.27 mm) can achieve a SE_T of ~43 dB. The shielding effectiveness can be further enhanced by GAFF stacking. For example, the EMI shielding cabinet made of 3 layers of GAFFs (total thickness of ~0.87 mm) showed SE_T up to ~85 dB. Traditional graphene-based materials used for EMI shielding typically include graphene aerogels[54,55], films[56], foams[57], and composites of graphene with CNTs[58], MXene[59], Fe_3O_4[60], or polymers[61–67]. Due to the limitations of material selection and preparation technologies, traditional graphene-based EMI shielding materials typically exhibit poor balance between thickness, shielding effectiveness, waveband, and mechanical strength (see more details in Supplementary Table 2). In contrast, GAFF addresses these issues by offering thin thickness, lightweight nature, high strength, high shielding effectiveness, and broad waveband. These characteristics well align with the high requirements of advanced EMI shielding materials in increasingly complicated electromagnetic environment. In addition, metallic- or magnetic-nanoparticle-modified fiber materials have also been widely developed as EMI shielding materials[68–72]. Compared with these materials, GAFF offers comprehensive advantages including high EMI shielding effectiveness, wide waveband, thin thickness, high mechanical strength, and service stability (see more details in Supplementary Table 3), which make it a promising material for applications in EMI shielding fields, integrating both structural and functional benefits.

Mass production of GAFF

The mass production of graphene materials is the foundation for the practical applications. In this work, beyond the laboratory-level preparation of GAFF, the stable mass production of this material was also successfully realized. Taking advantage of the lightweight, flexible, and high-strength features of GAFF, a home-made continuous roll-to-roll CVD growth system was designed as shown in Fig. 5a and Supplementary Fig. 23. This equipment included the unwinding unit (left), CVD furnace (with width ~21 cm and length ~210 cm), and rewinding unit (right). During the preparation process, the AFF (width of ~20 cm) was continuously introduced from the unwinding unit into the CVD furnace at a stable speed to complete the high-temperature deposition of graphene, and then the formed GAFF was collected in the rewinding unit. Note that during this dynamic process, different positions on the fabric experienced the same flow field and thermal field environment, which greatly ensured the growth uniformity of graphene. To our knowledge, the roll-to-roll CVD growth of graphene has been greatly developed on the copper foils[73,74], which provided valuable references for the development of the roll-to-roll system for GAFF mass production. Notably, due to the distinctive growth behaviors of graphene on the non-catalytic nonmetallic AFF substrate, some improvements have been made accordingly in the GAFF roll-to-roll system. For example, due to the absence of the catalytic capability of the AFF substrate, a much lower graphene growth rate than that on catalytic copper foil has resulted. To get graphene films with the specific thickness, a relatively long growth time was usually consumed, so the conveying speed of the

https://doi.org/10.1038/s41467-024-51118-x

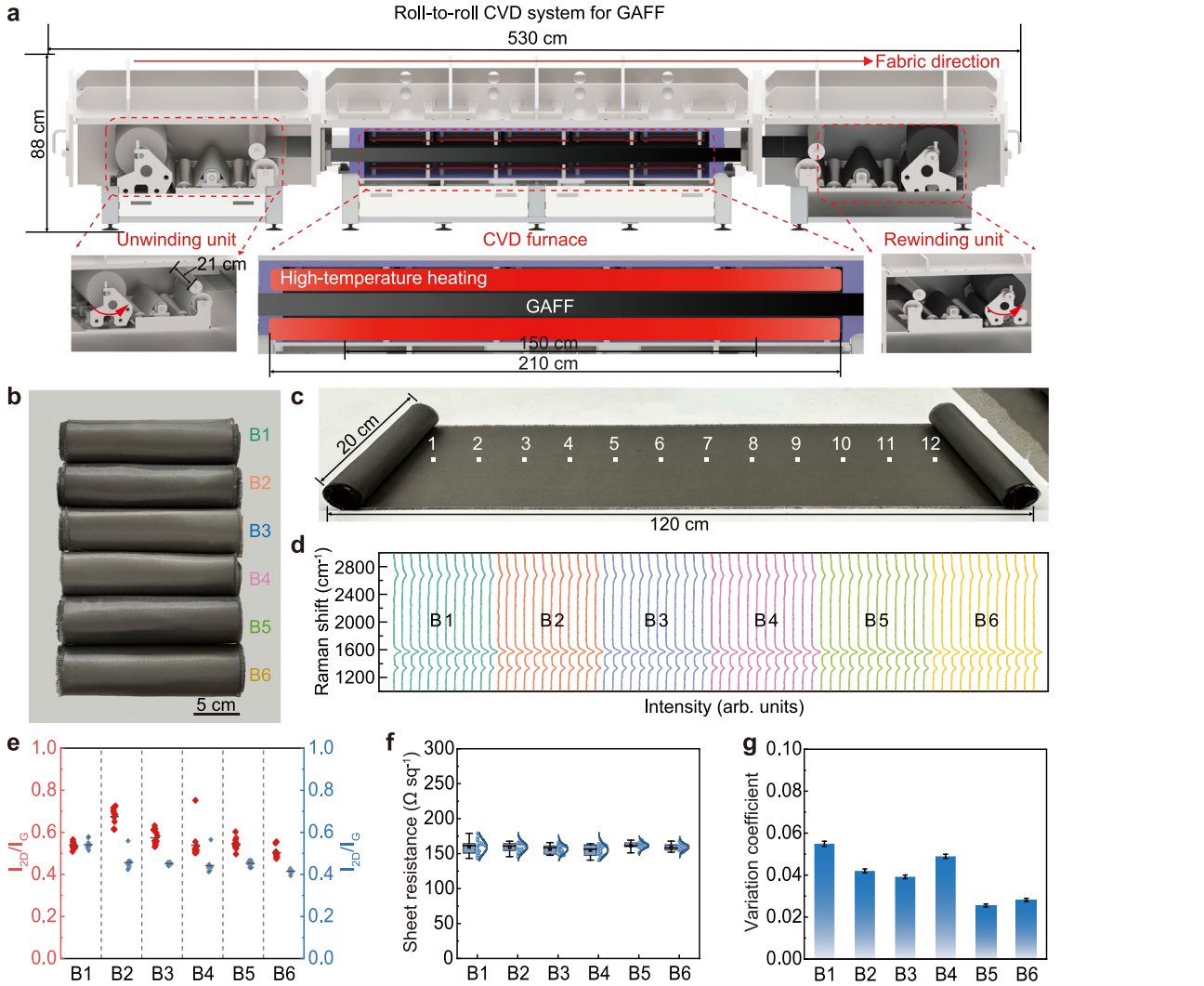

Fig. 5 | Mass production of GAFF with the home-made roll-to-roll CVD growth system. a Schematic diagram of home-made roll-to-roll equipment for mass production of GAFF. Arrows represented the direction of movement of the unwinding/rewinding unit. **b** Photograph of 6 batches of GAFFs with width of ~20 cm and length of ~2 m. **c** Photograph of the unfolded GAFF from B1. **d** Raman spectra of 6 batch GAFFs in **b**. 12 evenly-spaced positions were collected on each GAFF as marked in **c** with the internal of ~10 cm. **e** I_D/I_G and I_{2D}/I_G statistics of Raman spectra in **d**. **f**, **g** Sheet resistance statistics (**f**) and corresponding variation coefficient (**g**) of GAFFs in **b**. The error bars represent the standard deviations (n = 5). Gowth conditions in **b**–**g**: 400 sccm CH_4, 200 sccm H_2, ~1050 °C, and the rotation speed of ~60 mm min^{-1}.

fabric has to be well controlled very slow (graphene growth time in CVD system = length of heating zone of CVD chamber/conveying speed of fabric). During graphene growth, the slight change in growth time will cause the obvious fluctuation of graphene depositing thickness, and thus affect the uniformity of the obtained fabric. During the applications of GAFF, the sheet resistance was one of the significant factors considered, which is largely affected by the thickness of graphene, and usually requires to be modulated in a wide range according to precritical scenarios. Therefore, the conveying speed of the fabric in the roll-to-roll system was required to be regulated in a wide range with high accuracy. In our home-made system, the feed-back module was integrated to realize the real-time monitoring and dynamic controlling of the fabric conveying speed. In addition, a real-time sheet resistance detection module was also built in, which can guide the dynamic fine tuning of the rolling speed to ensure the uniformity of the obtained conductive fabric. Based on the current preparation process, our roll-to-roll growth system of GAFF can achieve an annual production capacity in the range of 468-936000 m^2 depending on the specifications of GAFF (more details in Supplementary Note 1).

The scale preparation processes of large-area GAFF (width of ~20 cm, length of ~2 m) have been successfully developed, where the excellent intra- and inter-batch repeatability and stability were successfully achieved (Fig. 5b). Figure 5c shows the GAFF from batch 1 (B1), which has high flexibility and can be folded and unfolded easily. The large-scale GAFF presented uniform contrast, and the high uniformity was further confirmed by the Raman characterizations. Figure 5d shows the Raman spectra of 6 batches of GAFFs in Fig. 5b (12 evenly-spaced positions collected on each GAFF, as marked in Fig. 5c, which showed consistent peak shapes of intra and inter batches. The corresponding statistics of I_D/I_G and I_{2D}/I_G in Fig. 5e further indicated the uniform crystal quality and layer thickness of the obtained graphene, confirming the high intra- and inter-batch stability and repeatability of our production process. In addition, Fig. 5f showed the sheet resistances of GAFF in each batch, which showed high consistency of intra- and inter-batches with a variation coefficient of <0.06 (Fig. 5g), where the collection details were similar to Supplementary Fig. 13, while the length was ~120 cm and the spacing was ~10 cm here. Now, for GAFF, its mass production beyond the laboratory level preparation has been

successfully realized, which will provide a solid foundation for the industrial application of this material.

Discussion

Graphene CVD growth on catalytic metal substrates holds promise for the mass production of high-quality graphene, however, its practical application remains hindered by the complicated subsequent peeling-transfer process onto target-using substrates. In this study, GAF/GAFF was pioneered through direct graphene CVD growth on commercially available nonmetallic AF/AFF substrates. Notably, during graphene growth on γ-Al_2O_3-AF, a distinctive VSS growth model of graphene was first revealed on a nonmetallic substrate, which contrasts with the well-known VS growth model observed on conventional catalytically inert nonmetallic substrates, leading to relatively fast and low-temperature graphene growth. The proposed VSS growth model significantly advanced our comprehension of graphene CVD growth on nonmetallic substrates. Beyond the laboratory-level preparation of GAFF, the stable mass production of large-scale GAFF was also achieved. This accomplishment establishes a solid foundation for the industrialization of this material. The obtained GAFF is characterized with a hierarchical conductive configuration, high strength, lightweight, flexibility, and thin thickness, positioning it as a promising advanced material for diverse applications, such as electrical heating and EMI shielding. The design strategy behind GAF/GAFF introduces an innovative approach to the development of graphene materials, where atomically thin graphene can hitch a ride on commercially used engineering material carriers to realize the practical applications.

Methods

CVD growth of GAF, GAFF, GQF, and GQFF

AF (F-72 type) and AFF (2626-P) used for graphene CVD growth were purchased from Rongrong New Materials Company, China. QF (Z/QC288) and QFF (Z/QWX200P) were purchased from Zhongtianjunda Company, China. Before graphene growth, AF, AFF, QF, and QFF were loaded into a quartz tube (inner diameter, 3.0 inch) of a three-zone furnace (Lindberg/Blue M Three-Zone Solid Tube Furnaces, Thermo Scientific, USA). The heating temperature of the chamber was set to ~800 °C, and the air was pumped for ~2 h for the removal of coated polymers.

In the graphene CVD growth progress, a consistent flow of 500 sccm Ar was introduced into the chamber during the temperature-raising stage, which was maintained throughout the entire CVD process. Upon the chamber reaching the target temperature (~800, ~900, ~1000, or ~1050 °C), a controlled flow of 500 sccm Ar, 4-500 sccm CH_4, and 200 sccm H_2 was initiated into the CVD chamber until graphene growth was completed, typically lasting 1–300 min. Subsequently, CH_4 and H_2 were ceased, and the heating was turned off. The chamber commenced cooling, during which only 500 sccm Ar was maintained. Once the furnace chamber reached room temperature, the Ar flow was turned off, and the sample was taken out. In experiments where QFF served as a control group for AFF, both substrates were positioned at the same depth within the quartz tube.

Transfer process for graphene thickness measurement

GAF or GAFF was cut into small pieces and diffused in 50% HF solution for hours to remove inside the fiber core. Afterward, the collapsed graphene ribbons coated on fiber were washed with deionized water three times. Finally, the graphene ribbons were loaded onto a silicon wafer or TEM grid and dried by an infrared lamp. The obtained samples can be used for the measurement of graphene thickness.

Characterizations

The samples were characterized using Raman spectroscopy (Horiba, LabRAM HR-800, laser excitation wavelength of 532 nm, 50× objective lens), SEM (FEI Quattro S, operating at 10 kV), HR-TEM (JEOL COM, JEM 2100 F, 200 kV), AFM (Bruker Dimension Icon with tapping mode), XRD (D8 Bruker, Cu Kα radiation), Py-IR (TENSOR 27 Bruker), four-point probe resistivity measurement system (RTS-8), electrical conductivity testing (Keithley 2400, Tektronix), tensile testing (MTS E43.104), SE_T testing (Keysight N5242B), infrared emission spectra and thermal radiation efficiency testing (Fourier transform infrared spectrometer of IRTracer-100, Fluke Ti 10 infrared camera), and temperature profile (direct-current power source, Fluke Ti 10 infrared camera).

The statistical data in Fig. 2b–d were collected by repeating the CVD experiment three times at each time point of ~20, ~30, ~40, ~60, ~70, ~80, ~120, ~130, ~140, ~150, ~160, ~180, ~200, ~210, and ~230 min for GAF together with GQF. Their surface morphology was characterized by SEM. The nucleation density and domain size were analyzed using Nano measurer, and the graphene coverage was estimated using statistical pixel values via Photoshop.

In the tensile test of graphene alumina fiber (GAF) in our study, we employed an electronic universal material testing machine with the model of MTS E43.104, as shown in Supplementary Fig. 15a. The tensile strength testing process can be divided into two steps: sample preparation and tensile strength test. To be specific: 1. Sample preparation: take an auxiliary plate The tensile strength testing process can be divided into two steps: sample preparation and tensile strength test. To be specific: 1. Sample preparation: Take an auxiliary plate (with a size of 20 mm × 40 mm, and a thickness of ~0.1 mm) made from paper, and cut a slot (~10 mm in width and ~30 mm in length) in the middle of the auxiliary plate (left of Supplementary Fig. 15b). This slot will accommodate the fiber bundle during testing. Take a fiber bundle with a length exceeding 30 mm, and place it in the center of the slot. Gently stretch the fiber bundle to ensure it is suspended and straight within the slot without bending. Next, fix the two ends of the fiber bundle onto the auxiliary plate with glue (middle of Supplementary Fig. 15b and left of Supplementary Fig. 15c). Then, carefully put the upper auxiliary plate over the fiber bundle and press it down firmly to secure the bundle in place. After curing for 24 h at room temperature and atmospheric conditions, align the specimen with the loading axis of the universal testing machine, and securely clamp the specimen in place to ensure proper alignment during the tensile test (middle of Supplementary Fig. 15c). Before applying a load, verify that the sample is not under any stress. Then, carefully cut off both sides of the auxiliary plate (right of Supplementary Fig. 15b and right of Supplementary Fig. 15c), and the sample is ready for the tensile test. 2. Tensile strength test: After confirming that the fiber sample remains intact and properly positioned, begin the equipment to load the sample at the set tensile speed (10 mm min^{-1}) until it is invalid. The breaking point represents the maximum stress that the bundle can withstand before fracturing. According to the peak stress (P) before the fiber bundle failure, the maximum tensile strength (σ) can be calculated by:

$$\sigma = P/A \tag{2}$$

where σ is the tensile strength (GPa), P is the breaking load (N), and A is the cross-sectional area of GAF bundle (mm^2), which is calculated by the ratio of linear density (0.0023 g cm^{-1}) to bulk density (2.9 g cm^{-3}), and calculated to be ~0.08 mm^2 for GAF bundle.

SE_T of GAFF was measured based on the coaxial transmission line method using a vector network analyzer (Keysight N5242B) as shown in Supplementary Fig. 22. GAFF was cut into 1 cm × 2 cm sample to fit the coaxial clamp in the testing system. The prepared sample was then placed in the center of the coaxial clamp. After the sample was securely fixed, the network vector analyzer was connected to initiate the test. Subsequently, the scattering parameters (S-parameters), including S_{11}, S_{21}, S_{12}, and S_{22}, were directly obtained after measurement, describing the frequency domain characteristics of the transmission channel. S_{11} is the input reflection coefficient (or input return loss), S_{21} is the forward transmission coefficient, S_{12} is the reverse transmission

coefficient, and S_{22} is the output reflection coefficient (or output return loss). For SE_T, it can be calculated from the measured S_{21} value, where:

$$SE_T = 10\log\left(\frac{1}{|S_{21}|^2}\right) \quad (3)$$

Computational methods

All calculations were based on density functional theory (DFT) and executed by the Vienna ab initio Simulation Package (VASP)[75]. The projected augmented wave (PAW) method was used for the interaction between valence electrons and ion cores. The exchange-correlation function was considered by the generalized gradient approximation (GGA) and Perdew-Burke-Ernzerhof (PBE) methods[76]. The energy cut-off of the plane wave basis was 450 eV. All structures were fully relaxed, and the energy and force converge were 10^{-4} eV and 0.05 eV/Å, respectively. The vacuum space between the images was set to be larger than 20 Å, to avoid the interaction between two adjacent images. The effects of graphene edges and free radicals were fully considered using spin-polarized calculations. The van der Waals (vdW) DFT, DFT-D2 method[77] within the framework of the PBE exchange-correlation function, was adopted to provide more accurate data.

We constructed a unit cell of γ-Al_2O_3 (110) and p (3 × 3) SiO_2 (0001) surfaces (see Supplementary Figs. 7 and 8 for detailed configurations) to investigate the adsorption and dehydrogenation of CH_4, respectively. The k-point meshes used in the relaxation calculations for the Brillouin zone integration were set as 2 × 2 × 1.

To simulate the kinetic process of graphene edge growth, ZZ and AC graphene nanoribbons with unit cells of 19.7 × 8.47 Å (AC) and 9.8 × 16.9 Å (ZZ) were constructed, respectively. Due to the large size of supercells, 1 × 2 × 1 and 2 × 1 × 1 k-point grids were used, respectively. We calculated the energy barriers for each reaction using the climbing image nudged elastic band (CI-NEB) method[78]. The transition states during each elementary reaction were verified by transition state imaginary frequency calculations. In order to ensure the accuracy of subsequent electronic property calculations of ELF, double meshes of k-points were employed to sample the Brillouin zones.

Data availability

The Source Data underlying the figures of this study are available with the paper. All raw data generated during the current study are available from the corresponding authors upon request. Source data are provided with this paper.

References

1. Li, X. S. et al. Large-area synthesis of high-quality and uniform graphene films on copper foils. *Science* **324**, 1312–1314 (2009).
2. Xu, X. et al. Ultrafast growth of single-crystal graphene assisted by a continuous oxygen supply. *Nat. Nanotechnol.* **11**, 930–935 (2016).
3. Shang, S. et al. A one-dimensional conductive metal-organic framework with extended π-d conjugated nanoribbon layers. *Nat. Commun.* **13**, 7599 (2022).
4. Reina, A. et al. Large area, few-layer graphene films on arbitrary substrates by chemical vapor deposition. *Nano Lett.* **9**, 30–35 (2009).
5. Li, X. S. et al. Evolution of graphene growth on Ni and Cu by carbon isotope labeling. *Nano Lett.* **9**, 4268–4272 (2009).
6. Gao, J. et al. Formation of carbon clusters in the initial stage of chemical vapor deposition graphene growth on Ni(111) surface. *J. Phys. Chem. C* **115**, 17695–17703 (2011).
7. Song, Y. et al. Graphene transfer: paving the road for applications of chemical vapor deposition graphene. *Small* **17**, 2007600 (2021).
8. Lin, L. et al. Bridging the gap between reality and ideal in chemical vapor deposition growth of graphene. *Chem. Rev.* **118**, 9281–9343 (2018).
9. Bao, W. et al. Controlled ripple texturing of suspended graphene and ultrathin graphite membranes. *Nat. Nanotechnol.* **4**, 562–566 (2009).
10. Cui, G. et al. Massive growth of graphene quartz fiber as a multifunctional electrode. *ACS Nano* **14**, 5938–5945 (2020).
11. Yuan, H. et al. Dual-Emitter graphene glass fiber fabric for radiant heating. *ACS Nano* **16**, 2577–2584 (2022).
12. Zhou, X. et al. The rise of graphene photonic crystal fibers. *Adv. Funct. Mater.* **32**, 2202282 (2022).
13. Sun, J. et al. Graphene glass from direct CVD routes: production and applications. *Adv. Mater.* **28**, 10333–10339 (2016).
14. Cui, G. et al. Freestanding graphene fabric film for flexible infrared camouflage. *Adv. Sci.* **9**, 961–968 (2021).
15. Cheng, Y. et al. Controllable growth of graphene photonic crystal fibers with tunable optical nonlinearity. *ACS Photon.* **9**, 961–968 (2022).
16. Cheng, Y. et al. Graphene infrared radiation management targeting photothermal conversion for electric-energy-free crude oil collection. *J. Am. Chem. Soc.* **144**, 15562–15568 (2022).
17. Moser, B. et al. Nextel (TM) 610 alumina fibre reinforced aluminium: influence of matrix and process on flow stress. *Compos. Part. A-Appl. Sci. Manuf.* **32**, 1067–1075 (2001).
18. Li, L. et al. Research progress of ultrafine alumina fiber prepared by sol-gel method: a review. *Chem. Eng. J.* **421**, 127744 (2021).
19. Cheng, T. et al. The Mechanism of graphene vapor-solid growth on nonmetallic substrates. *ACS Nano* **15**, 7399–7408 (2021).
20. Ismach, A. et al. Direct chemical vapor deposition of graphene on dielectric surfaces. *Nano Lett.* **10**, 1542–1548 (2010).
21. Bachmatiuk, A. et al. Investigating the graphitization mechanism of SiO_2 nanoparticles in chemical vapor deposition. *ACS Nano* **3**, 4098–4104 (2009).
22. Wang, H. et al. Primary nucleation-dominated chemical vapor deposition growth for uniform graphene monolayers on dielectric substrate. *J. Am. Chem. Soc.* **141**, 11004–11008 (2019).
23. Liu, F. et al. Achievements and challenges of graphene chemical vapor deposition growth. *Adv. Funct. Mater.* **32**, 22031 (2022).
24. Shan, J. et al. Chemical vapor deposition synthesis of graphene over sapphire substrates. *ChemNanoMat* **7**, 515–525 (2021).
25. Fan, X. et al. Spontaneous folding growth of graphene on h-BN. *Nano Lett.* **21**, 2033–2039 (2021).
26. Wang, M. et al. A platform for large-scale graphene electronics-CVD growth of single-layer graphene on CVD-grown hexagonal boron nitride. *Adv. Mater.* **25**, 2746–2752 (2013).
27. Ding, X. et al. Direct growth of few layer graphene on hexagonal boron nitride by chemical vapor deposition. *Carbon* **49**, 2522–2525 (2011).
28. Jiang, B. et al. Toward direct growth of ultra-flat graphene. *Adv. Funct. Mater.* **32**, 2200428 (2022).
29. Khan, A. et al. Direct CVD growth of graphene on technologically important dielectric and semiconducting substrates. *Adv. Sci.* **5**, 1800050 (2018).
30. Chen, Z. et al. Direct CVD growth of graphene on traditional glass: methods and mechanisms. *Adv. Mater.* **31**, 1803639 (2019).
31. Cheng, Y. et al. Chemical vapor deposition method for graphene fiber materials. *Acta Phys. -Chim. Sin.* **38**, 2006046 (2020).
32. Liu, R. et al. Complementary chemical vapor deposition fabrication for large-area uniform graphene glass fiber fabric. *Small Methods* **6**, 2200499 (2022).
33. Ma, T. et al. Repeated growth-etching-regrowth for large-area defect-free single-crystal graphene by chemical vapor deposition. *ACS Nano* **8**, 12806–12813 (2014).

34. Xie, Y. et al. Ultrafast catalyst-free graphene growth on glass assisted by local fluorine supply. *ACS Nano* **13**, 10272–10278 (2019).
35. Eres, G. et al. Cooperative island growth of large-area single-crystal graphene on copper using chemical vapor deposition. *ACS Nano* **8**, 5657–5669 (2014).
36. Kim, H. et al. Activation energy paths for graphene nucleation and growth on Cu. *ACS Nano* **6**, 3614–3623 (2012).
37. Ferrari, A. C. & Basko, D. M. Raman spectroscopy as a versatile tool for studying the properties of graphene. *Nat. Nanotechnol.* **8**, 235–246 (2013).
38. Digne, M. et al. Use of DFT to achieve a rational understanding of acid-basic properties of γ-alumina surfaces. *J. Catal.* **226**, 54–68 (2004).
39. Lagauche, M. et al. Thermodynamic characterization of the hydroxyl group on the γ-alumina surface by the energy distribution function. *J. Phys. Chem. C* **121**, 16770–16782 (2017).
40. Köhler, C. et al. Theoretical investigation of carbon defects and diffusion in α-quartz. *Phys. Rev. B* **64**, 085333 (2001).
41. Wang, C. et al. Continuous synthesis of graphene nano-flakes by a magnetically rotating arc at atmospheric pressure. *Carbon* **148**, 394–402 (2019).
42. Cholewinski, M. C. et al. Computational study of methane activation on γ-Al_2O_3. *ACS Omega* **3**, 18242–18250 (2018).
43. Wischert, R. et al. γ-Alumina: the essential and unexpected role of water for the structure, stability, and reactivity of "defect" sites. *J. Am. Chem. Soc.* **134**, 14430–14449 (2012).
44. Park, J. et al. Growth, quantitative growth analysis, and applications of graphene on γ-Al_2O_3 catalysts. *Sci. Rep.* **5**, 11839 (2015).
45. Singh, P. et al. Assessing the effect of dopants on the C-H activation activity of γ-Al_2O_3 using first-principles calculations. *Chemphyschem* **24**, e202200670 (2023).
46. Habib, M. R. et al. A review of theoretical study of graphene chemical vapor deposition synthesis on metals: nucleation, growth, and the role of hydrogen and oxygen. *Rep. Prog. Phys.* **81**, 036501 (2018).
47. Yamamoto, M. et al. Porous nanographene formation on γ-alumina nanoparticles via transition-metal-free methane activation. *Chem. Sci.* **13**, 3140–3146 (2022).
48. Ivanov, R. et al. Graphene-encapsulated aluminium oxide nanofibers as a novel type of nanofillers for electroconductive ceramics. *J. Eur. Ceram. Soc.* **35**, 4017–4021 (2015).
49. Zhao, Q. et al. The carbon chain growth during the onset of CVD graphene formation on γ-Al_2O_3 is promoted by unsaturated CH_2 ends. *Phys. Chem. Chem. Phys.* **24**, 23357–23366 (2022).
50. Blanc, D. et al. Study and modelling of coated car painting film by infrared or convective drying. *Dry. Technol.* **15**, 2303–2323 (1997).
51. Dufour, P. et al. Infrared drying process of an experimental water painting: Model predictive control. *Dry. Technol.* **22**, 269–284 (2004).
52. Wei, Q. et al. Superhigh electromagnetic interference shielding of ultrathin aligned pristine graphene nanosheets film. *Adv. Mater.* **32**, e1907411 (2020).
53. Xie, Y. et al. Ultra-Broadband strong electromagnetic interference shielding with ferromagnetic graphene quartz fabric. *Adv. Mater.* **34**, e2202982 (2022).
54. Xi, J. et al. Graphene aerogel films with expansion enhancement effect of high-performance electromagnetic interference shielding. *Carbon* **135**, 44–51 (2018).
55. González, M. et al. Modulating the electromagnetic shielding mechanisms by thermal treatment of high porosity graphene aerogels. *Carbon* **147**, 27–34 (2019).
56. Shen, B. et al. Ultrathin flexible graphene film: an excellent thermal conducting material with efficient EMI shielding. *Adv. Funct. Mater.* **24**, 4542–4548 (2014).
57. Shen, B. et al. Microcellular graphene foam for improved broadband electromagnetic interference shielding. *Carbon* **102**, 154–160 (2016).
58. Kong, L. et al. Powerful absorbing and lightweight electromagnetic shielding CNTs/RGO composite. *Carbon* **145**, 61–66 (2019).
59. Fan, Z. et al. A lightweight and conductive MXene/graphene hybrid foam for superior electromagnetic interference shielding. *Chem. Eng. J.* **381**, 122696 (2020).
60. Song, W.-L. et al. Magnetic and conductive graphene papers toward thin layers of effective electromagnetic shielding. *J. Mater. Chem. A* **3**, 2097–2107 (2015).
61. Wang, L. et al. Lightweight and robust rGO/sugarcane derived hybrid carbon foams with outstanding EMI shielding performance. *J. Mater. Sci. Technol.* **52**, 119–126 (2020).
62. Vu, M. C. et al. Hybrid shell of MXene and reduced graphene oxide assembled on PMMA bead core towards tunable thermoconductive and EMI shielding nanocomposites. *Compos. Part A-Appl. Sci. Manuf.* **149**, 106574 (2021).
63. Liang, C. et al. Superior electromagnetic interference shielding 3D graphene nanoplatelets/reduced graphene oxide foam/epoxy nanocomposites with high thermal conductivity. *J. Mater. Chem. C* **7**, 2725–2733 (2019).
64. Barani, Z. et al. Multifunctional graphene composites for electromagnetic shielding and thermal management at elevated temperatures. *Adv. Electron. Mater.* **6**, 2000520 (2020).
65. Shi, S. et al. 3D printed polylactic acid/graphene nanocomposites with tailored multifunctionality towards superior thermal management and high-efficient electromagnetic interference shielding. *Chem. Eng. J.* **450**, 138248 (2022).
66. Chen, Z. et al. Lightweight and flexible graphene foam composites for high-performance electromagnetic interference shielding. *Adv. Mater.* **25**, 1296–1300 (2013).
67. Li, J. et al. Bubble-templated rGO-graphene nanoplatelet foams encapsulated in silicon rubber for electromagnetic interference shielding and high thermal conductivity. *Chem. Eng. J.* **415**, 129504 (2021).
68. Ren, W. et al. Flexible and robust silver coated non-woven fabric reinforced waterborne polyurethane films for ultra-efficient electromagnetic shielding. *Compos. Part B-Eng.* **184**, 107745 (2020).
69. Zhang, S. et al. Polyvinylpyrrolidone assisted preparation of highly conductive, antioxidation, and durable nanofiber composite with an extremely high electromagnetic interference shielding effectiveness. *ACS Appl. Mater. Interfaces* **13**, 21865–21875 (2021).
70. He, D. et al. Durable cellulose paper by grafting thiol groups and controlling silver deposition for ultrahigh electromagnetic interference shielding. *Int. J. Biol. Macromol.* **248**, 125972 (2023).
71. Huang, J. et al. Lightweight and textured Ni@Cu-encapsulated carbon tube with outstanding electromagnetic interference shielding performance. *Compos. Sci. Technol.* **228**, 109636 (2022).
72. Movassagh-Alanagh, F. et al. Three-phase PANI@nano-Fe_3O_4@CFs heterostructure: Fabrication, characterization and investigation of microwave absorption and EMI shielding of PANI@nano-Fe_3O_4@CFs/epoxy hybrid composite. *Compos. Sci. Technol.* **150**, 65–78 (2017).
73. Bae, S. et al. Roll-to-roll production of 30-inch graphene films for transparent electrodes. *Nat. Nanotechnol.* **5**, 574–578 (2010).
74. Deng, B., Liu, Z. & Peng, H. Toward mass production of CVD graphene films. *Adv. Mater.* **31**, 1800996 (2018).
75. Kresse, G. & Furthmuller, J. Efficient iterative schemes for ab initio total-energy calculations using a plane-wave basis set. *Phys. Rev. B* **54**, 11169–11186 (1996).
76. Hammer, B. et al. Improved adsorption energetics within density-functional theory using revised Perdew-Burke-Ernzerhof functionals. *Phys. Rev. B* **59**, 7413–7421 (1999).

77. Grimme, S. Semiempirical GGA-type density functional constructed with a long-range dispersion correction. *J. Comput. Chem.* **27**, 1787–1799 (2006).
78. Henkelman, G. et al. A climbing image nudged elastic band method for finding saddle points and minimum energy paths. *J. Chem. Phys.* **113**, 9901–9904 (2000).

Acknowledgements

This work was financially supported by the National Natural Science Foundation of China (NSFC. Nos. T2188101, 52272032, and 52021006), and the Beijing Nova Program of Science and Technology (No.20220484079).

Author contributions

W.J.L., F.S.L, and X.C.S. conceived the project and designed the experiment. W.J.L. and F.S.L. manufactured these devices with the assistance of K.Y.Z., R.J.L., H.Y., Y.C., J.N.W., and X.Y.M.; measurements were made by W.J.L. and F.S.L. with the assistance of K.W.H., K.W., S.T.C., Y.C., Y.Y.Y., C.T., K.Y.Z., F.Y., W.J.Y., A.L.C., and X.B.W.; X.C.S. carried out DFT simulations. W.J.L., F.S.L., and X.C.S. co-wrote the paper under the guidance of Y.Q. and Z.F.L. All authors contributed to the discussion and analysis of the results.

Competing interests

The authors declare no competing interests.

Additional information

Supplementary information The online version contains supplementary material available at https://doi.org/10.1038/s41467-024-51118-x.

Correspondence and requests for materials should be addressed to Yue Qi or Zhongfan Liu.

Peer review information *Nature Communications* thanks the anonymous reviewers for their contribution to the peer review of this work. A peer review file is available.

[1]Centre for Nanochemistry, Beijing Science and Engineering Centre for Nanocarbons, Beijing National Laboratory for Molecular Sciences, College of Chemistry and Molecular Engineering, Peking University, Beijing, China. [2]Beijing Graphene Institute (BGI), Beijing, China. [3]College of Energy, Soochow Institute for Energy and Materials Innovations (SIEMIS), Jiangsu Provincial Key Laboratory for Advanced Carbon Materials and Wearable Energy Technologies, Soochow University, Suzhou, China. [4]State Key Laboratory of Heavy Oil Processing, College of Science, China University of Petroleum, Beijing, China. [5]Department of Chemistry, College of Chemistry and Materials Engineering, Beijing Technology and Business University, Beijing, China. [6]These authors contributed equally: Wenjuan Li, Fushun Liang, Xiucai Sun. ✉e-mail: qiyue@bgi-graphene.com; zfliu@pku.edu.cn